buildings

MDPI

Article

A Double-Hardening Elastoplastic Load-Transfer Model for Assessing Load-Carrying Performance of Axially Loaded Piles

Yexun Li [1], Yunzhe Zhang [2], Haoyu Liu [2,*], Xian Wang [1], Song Qiu [1], Jian Yu [3] and Lin Li [2]

[1] CCCC, Third Harbour Engineering Corporation Ltd., Shanghai 200032, China; liyexun@ccccltd.cn (Y.L.); wangxian5@ccccltd.cn (X.W.); qiusong@ccccltd.cn (S.Q.)
[2] School of Highway, Chang'an University, Xi'an 710064, China; 2024121081@chd.edu.cn (Y.Z.); linli_chd@chd.edu.cn (L.L.)
[3] Department of Civil Engineering, Tongji University, Shanghai 200092, China; 002yujian@tongji.edu.cn
* Correspondence: 2025221221@chd.edu.cn

Abstract

Accurate prediction of the load–settlement response of axially loaded piles remains challenging because the pile–soil interface undergoes progressive elastoplastic shear deformation accompanied by stress-dependent volumetric changes. Conventional one-dimensional load-transfer models are computationally efficient but usually rely on empirical or hyperbolic fitting functions, making it difficult to explicitly describe the coupled evolution of interface shear hardening, volumetric hardening, and radial effective stress. Although three-dimensional elastoplastic models provide a more rigorous mechanical representation, their high computational cost limits routine engineering application. To address this gap, this study develops a double-hardening elastoplastic load-transfer model for axially loaded piles based on a physically interpretable pile–soil interface constitutive formulation. In the proposed model, the Hardening Soil model is used to characterize interface shear hardening, while the Modified Cam-clay model is introduced to describe volumetric hardening. These two mechanisms are coupled through a stress–dilatancy relationship. According to the loading direction and the position of the current stress point relative to the shear and volumetric yield surfaces, the p′–q stress plane is divided into elastic, shear-hardening, volumetric-hardening, and coupled double-hardening regions. The corresponding incremental constitutive equations are derived and embedded into a conventional load-transfer framework. The model is validated using interface direct shear tests and field-scale static pile load tests. The predicted shear stress–displacement curves and pile-head load–settlement responses agree well with the measured data. Quantitative evaluation shows that the MAPE values are lower than 5%, the maximum relative errors are below 7.6%, and the R^2 values exceed 0.96 for all validation cases.

Keywords: pile–soil interface; axially loaded piles; double-hardening elastoplastic model; load-transfer method; elastoplastic constitutive model; shear hardening; volumetric hardening; modified cam-clay model

Check for updates

Academic Editor: Harry Far

Received: 28 May 2026
Revised: 11 June 2026
Accepted: 17 June 2026
Published: 19 June 2026

Copyright: © 2026 by the authors. Licensee MDPI, Basel, Switzerland. This article is an open access article distributed under the terms and conditions of the Creative Commons Attribution (CC BY) license.

1. Introduction

The load-settlement behavior of pile foundations fundamentally governs the structural safety and serviceability of engineering projects. Accurately simulating the intricate deformation mechanisms at the pile–soil interface is essential for enhancing the reliability of pile bearing capacity assessments. Under service conditions, the significant disparity between the elastic moduli of the pile body and the surrounding soil leads to highly inconsistent

deformations across the contact surface. This kinematic mismatch generates substantial shear stresses, causing the interface shear deformation to exhibit pronounced elastoplastic characteristics [1]. Furthermore, as load-transfer occurs, the soil within the lateral shear deformation zone undergoes complex mechanical processes, specifically nonlinear shear response and volumetric hardening. Therefore, it is of critical scientific value and engineering significance to rigorously account for the elastoplastic deformation laws and load-transfer mechanisms of the pile–soil interface, thereby deriving a robust calculation method for the load-settlement response of axially loaded piles [2,3].

The load–settlement relationship serves as a primary indicator of a pile's deformation characteristics and bearing performance; thus, accurately simulating settlement under loading remains a pivotal challenge in foundation engineering. Early analytical frameworks were predominantly rooted in linear elastic theory, which inherently fails to account for the nonlinear constitutive properties of real-world soils [4,5]. While the shear displacement method offers a description of the soil deformation surrounding the pile, it typically idealizes the soil as an elastic medium, thereby struggling to capture the localized elastoplastic shear behavior at the pile–soil interface [6]. Similarly, the layer-wise summation method—though capable of accumulating individual layer compressions—is often constrained by oversimplified assumptions and localized parameters, frequently neglecting complex three-dimensional stress effects [7]. In contrast, the load-transfer method has gained widespread adoption in the mechanical analysis of single piles [8]. Its prominence stems from its computational efficiency, the versatility in selecting diverse transfer functions, and its capacity to incorporate soil stratification [9]. Given that the load-transfer function dictates the evolution of shaft friction relative to pile–soil displacement, it remains the decisive factor in the precision of load-settlement predictions [10]. However, conventional functions such as bilinear or hyperbolic models, while capable of approximating interaction, often involve parameters that are difficult to calibrate or yield solutions with high mathematical complexity [11]. More importantly, these mathematical curve-fitting functions lack a rigorous elastoplastic foundation, rendering them incapable of capturing the dynamic stress–state evolution surrounding the shaft [12].

The shear characteristics of the pile–soil interface are fundamental to shaft resistance, directly governing the overall bearing capacity and settlement–deformation response of pile foundations [13]. Early empirical interface models largely relied on oversimplified descriptions of shear deformation. For instance, Kraft et al. (1981) [14] introduced a nonlinear load-transfer function based on a hyperbolic stress–strain relationship, while Zhu et al. (2002) [15] derived modulus degradation curves validated by load test results. However, these models suffer from limited generalizability and lack clear physical interpretations for their parameters. As advanced soil mechanics progressed, elastoplastic frameworks featuring single or dual hardening parameters emerged to replace these empirical curves. Since the foundational development of the Cam-clay model [16], researchers have utilized plastic volumetric strain to control yield surface expansion, providing a superior description of soil compression behaviors [17]. Similarly, Xu et al. (2010) [18] established a constitutive model within the Mohr-Coulomb framework based on shear hardening rules to predict volumetric changes during shear. Nevertheless, a single hardening parameter inherently fails to account for the essential coupling effects between shear and volumetric yielding at the structure–soil boundary. To overcome these theoretical constraints, double-hardening constitutive concepts were developed. For instance, the well-known Hardening Soil (HS) framework incorporated both shear and cap yield surfaces to simulate nonlinear soil behavior under diverse stress paths [19]. Furthermore, Shen (1995) [20] utilized plastic volumetric and deviatoric strains as dual hardening parameters to simulate normally and

over-consolidated soils, while Yu et al. (2009) [21] modified double-hardening formulations to reflect cementation effects.

Recent studies have further advanced the analysis of pile–soil interaction and nonlinear pile load-settlement behavior from different perspectives. Bateman et al. [22] developed theoretical t–z curves for axially loaded piles, providing a more rigorous basis for interpreting shaft resistance mobilization. Sharo et al. [23] proposed a new approach for predicting the load-displacement response of axially loaded piles in sand, highlighting the importance of accurately characterizing nonlinear pile–soil interaction. Li et al. [24] developed a generalized elastoplastic load-transfer model for axially loaded piles in clay by incorporating modulus degradation and skin friction softening, demonstrating that degradation of shaft resistance should be considered under large loading levels. Pham et al. [25] further introduced a softening-based interface model for nonlinear load-settlement analysis of piles in saturated and unsaturated multi-layered soils, emphasizing the role of interface hardening–softening behavior in complex soil profiles. In addition to conventional circular piles, recent studies have extended load-transfer analysis to more complex engineering scenarios. Mao et al. [26] derived an analytical solution for axially loaded floating pipe piles, while Zhou et al. [27] developed a load-transfer model for vertically loaded non-circular piles, showing that pile geometry and pile type can significantly influence the construction of load-transfer relationships. Cesaro et al. [28] investigated the shaft resistance of bored piles in sand, further confirming the importance of accurately assessing shaft resistance mobilization. Meanwhile, Nguyen et al. [29] introduced a hybrid machine-learning framework for predicting load-displacement behavior of bored piles, indicating that data-driven methods have become an emerging tool for pile response prediction. Although these recent studies have improved the prediction of pile load-settlement behavior, most existing models still focus mainly on empirical curve fitting, shear softening, or shaft resistance mobilization. The coupled evolution of shear hardening, volumetric hardening, and radial effective stress at the pile–soil interface has not been sufficiently incorporated into a computationally efficient one-dimensional load-transfer framework [5]. Compared with existing pile load-transfer models, the distinction of the present study lies in the way the interface constitutive response is incorporated into the load-transfer formulation. Empirical and hyperbolic load-transfer models, such as conventional t–z curves, are computationally efficient but mainly depend on curve-fitting parameters and do not explicitly describe elastoplastic hardening. Modulus-degradation or softening-based models improve the nonlinear representation of shaft resistance, but they usually emphasize stiffness degradation, skin-friction softening, or resistance mobilization rather than the coupled evolution of shear and volumetric yielding. Existing elastoplastic interface models can provide stronger mechanical interpretation, but many of them are either based on a single hardening mechanism or formulated within relatively complex numerical frameworks. In contrast, the proposed model combines the shear-hardening mechanism of the Hardening Soil model and the volumetric-hardening mechanism of the Modified Cam-clay model through a stress–dilatancy relationship, and it further embeds this coupled interface response into a one-dimensional incremental load-transfer framework. Therefore, the main contribution of this study is not the introduction of a completely new soil plasticity theory, but the projection of a coupled double-hardening interface mechanism into an efficient pile settlement prediction framework with clearer physical interpretability than purely empirical transfer functions.

Despite these theoretical and methodological advances, the novelty of an efficient double-hardening load-transfer model for axially loaded piles still requires further clarification. Existing double-hardening constitutive models provide a rigorous description of soil plasticity, but they are generally formulated within three-dimensional numerical frameworks and are not directly suitable for routine one-dimensional pile settlement analy-

sis. Conventional load-transfer models are computationally efficient, but they commonly rely on empirical or hyperbolic transfer functions and therefore cannot explicitly describe the coupled evolution of interface shear hardening, volumetric hardening, and radial effective stress [30]. Existing interface constitutive models can characterize certain aspects of interface shear deformation or softening, but the coupled shear–volumetric hardening mechanism has not been sufficiently incorporated into an incremental load-transfer formulation for predicting pile load–settlement response.

Based on the above comparison, the theoretical gap addressed in this study is how to project the coupled double-hardening elastoplastic response of the pile–soil interface into a simplified but physically interpretable one-dimensional load-transfer framework. To bridge this gap, this study develops a double-hardening elastoplastic load-transfer model for axially loaded piles. The novelty of the proposed model lies in three aspects. First, the shear-hardening mechanism of the Hardening Soil model and the volumetric-hardening mechanism of the Modified Cam-clay model are coupled through a stress–dilatancy relationship to describe the pile–soil interface response [31]. Second, the p′–q stress plane is divided into elastic, shear-hardening, volumetric-hardening, and coupled double-hardening regions, and the corresponding incremental constitutive equations are derived according to the plastic consistency condition and flow rules [32]. Third, the derived interface constitutive relationship is embedded into a one-dimensional load-transfer framework by combining the elastoplastic shear displacement in the shear deformation zone with the elastic displacement of the surrounding soil [33,34]. This enables the nonlinear load–settlement response of axially loaded piles to be predicted with both mechanical interpretability and computational efficiency, providing a theoretical and practical basis for settlement analysis and bearing capacity assessment [35,36].

2. Methodology

2.1. Overview of the Proposed Framework

The overall methodological framework of this study is illustrated in Figure 1. The proposed framework begins with the development of a double-hardening elastoplastic constitutive model for the pile–soil interface. Four key components are considered in the model formulation: stress–dilatancy coupling, the shear-hardening mechanism, the definition of stress variables, and the volumetric-hardening mechanism. The shear-hardening behavior is described based on the Hardening Soil model, while the volumetric-hardening behavior is characterized using the Modified Cam-clay model. These two mechanisms are coupled through the stress–dilatancy relationship to represent the interaction between shear deformation and volumetric plastic deformation at the pile–soil interface.

Based on the defined stress variables and yield functions, the stress plane is further divided into four regions according to the relative position of the current stress point and the loading direction. These regions include the elastic region, the shear-hardening region, the volumetric-hardening region, and the coupled double-hardening region. For each region, the corresponding incremental constitutive equations are derived using the plastic consistency condition and the associated or non-associated flow rules.

The derived constitutive relationship is then implemented into a one-dimensional load-transfer framework. In this framework, the pile is discretized into a series of elements, and the shaft resistance, pile displacement, and pile-head load–settlement response are calculated through an incremental iterative procedure. Finally, the proposed model is validated using laboratory interface direct shear tests and field-scale static pile load tests. The validation results are used to assess the predictive accuracy of the model and to provide feedback for parameter calibration.

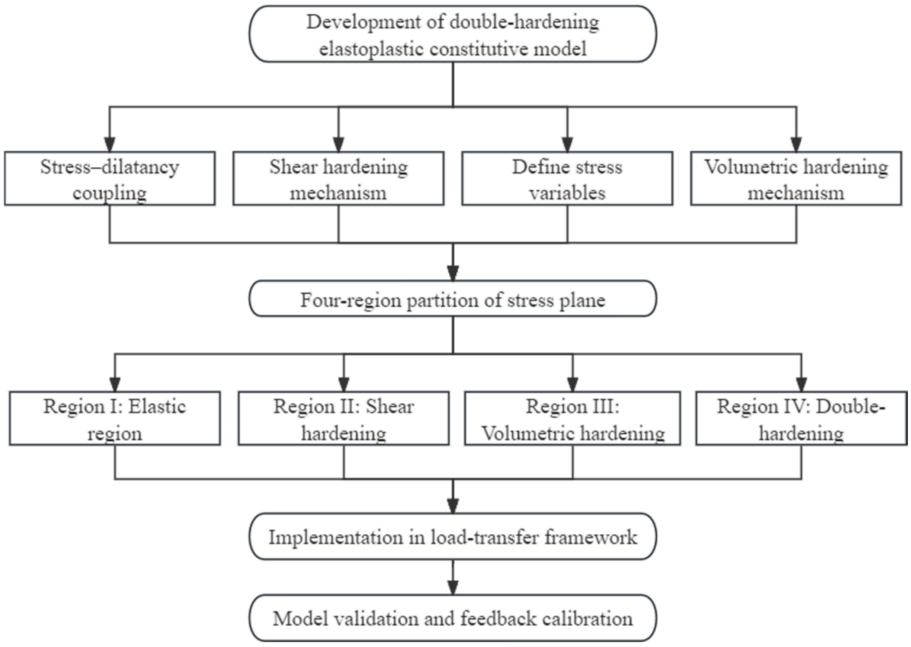


Figure 1. Schematic diagram of the overall methodological flowchart.

2.2. Double-Hardening Constitutive Model

2.2.1. Yield Functions

The deviatoric stress q and mean effective stress p' characterize the overall shear and compressive states of the soil, respectively. To facilitate the formulation of yield and hardening criteria, p' and q are utilized as the fundamental stress variables. By accounting for the coupled evolution of shear and volumetric hardening mechanisms, and adopting the plastic shear strain as the primary hardening parameter, the shear yield function of the Hardening Soil (HS) model is defined as follows [37]:

$$f^{\mathrm{s}} = \frac{q_{\mathrm{a}}}{E_{50}} \cdot \frac{q}{q_{\mathrm{a}} - q} - \frac{2q}{E_{\mathrm{ur}}} - \gamma_{\mathrm{p}} \tag{1}$$

where E_{50} and E_{ur} are the reference values of loading modulus and unloading–reloading modulus under the given confining pressure p^{ref}.

$$E_{50} = E_{50}^{\mathrm{ref}} \left(\frac{p' + c' \cos \varphi'}{p^{\mathrm{ref}} + c' \cos \varphi'} \right)^{\mathrm{m}} \tag{2}$$

$$E_{\mathrm{ur}} = E_{\mathrm{ur}}^{\mathrm{ref}} \left(\frac{p' + c' \cos \varphi'}{p^{\mathrm{ref}} + c' \cos \varphi'} \right)^{\mathrm{m}} \tag{3}$$

where c' is the effective cohesion of the soil; φ' cis the effective angle of internal friction; m is the exponent parameter fitted from triaxial test results.

Based on the Mohr-Coulomb criterion, the allowable deviatoric stress q_a is defined as:

$$q_{\mathrm{a}} = \frac{q_{\mathrm{f}}}{R_{\mathrm{f}}} = \frac{\sqrt{3}(p' \sin \varphi' + c' \sin \varphi')}{R_{\mathrm{f}} \left(\frac{1}{\sqrt{3}} \sin \theta \sin \varphi' + \cos \theta \right)} \tag{4}$$

where q_{f} is the ultimate deviatoric stress calculated based on the Mohr-Coulomb criterion; R_{f} is the failure ratio; θ is the Lode angle of stress.

Figure 2 illustrates the evolution of the shear yield surface in the $p' - q$ plane at various plastic shear strains γ^{p}. It depicts the expansion process wherein the yield surface enlarges following the shear yielding of the soil surrounding the pile until the critical state is attained.

In this context, f_0^s denotes the initial shear yield surface of the soil, while the Critical State Line (CSL) serves as the boundary for the pile–soil interface upon reaching the critical state under external loading.

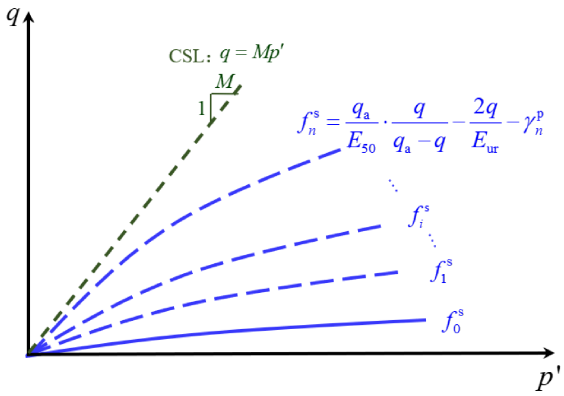


Figure 2. Schematic diagram of the expansion of shear yield surfaces.

The model adopts the plastic volumetric strain as the second hardening parameter. Within the framework of the Modified Cam-clay (MCC) model, the volumetric yield surface is formulated as follows:

$$f^c = q^2 - M^2 p'(p'_c - p') \tag{5}$$

where p'_c is the yield stress; M is the critical state stress ratio and can be expressed as:

$$M = \frac{3\sin\varphi'}{\sin\theta\sin\varphi' + \sqrt{3}\cos\theta} \tag{6}$$

The Modified Cam-clay (MCC) model adopts the plastic volumetric strain as the hardening parameter, and its differential relationship with the yield stress p'_c can be expressed as:

$$\mathrm{d}p'_c = \frac{1+e_0}{\lambda - k} p'_c \mathrm{d}\varepsilon_v^p \tag{7}$$

where e_0 is the initial void ratio; λ is the compression index; k is the swelling index.

Figure 3 illustrates the evolution of the volumetric yield surface associated with varying yield stresses p'_c. It depicts the evolutionary mechanism in which the yield surface progressively expands and eventually converges toward the critical state subsequent to the volumetric yielding of the interface soil. In this context, p'_{c0} denotes the pre-consolidation pressure corresponding to the initial volumetric yield surface.

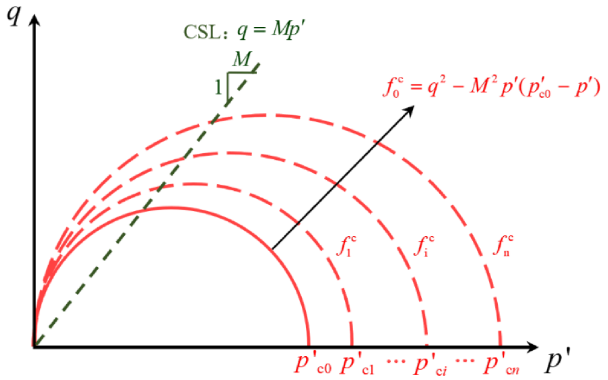


Figure 3. Schematic diagram of the expansion of volumetric yield surfaces.

Under the action of shear stress, soil exhibits volumetric dilation behavior. The stress-dilatancy equation describes the coupling relationship between shear hardening and volumetric hardening [38]. Based on the stress–dilatancy equation, the coupling relationship between the plastic shear strain increment $d\gamma^p$ and the plastic volumetric strain increment $d\varepsilon_v^p$ can be expressed as:

$$d\varepsilon_v^p = \frac{\sin\psi_m}{\frac{1}{\sqrt{3}}\sin\theta\sin\varphi' + \cos\theta} d\gamma^p \tag{8}$$

where ψ_m is expressed as:

$$\sin\psi_m = \frac{\sin\varphi_m - \sin\varphi_{cs}}{1 - \sin\varphi_m \sin\varphi_{cs}} \tag{9}$$

$$\sin\varphi_m = \frac{q}{p' - c'\cos\varphi'} \tag{10}$$

$$\sin\varphi_{cs} = \frac{\sin\varphi' - \sin\varphi'_p}{1 - \sin\varphi'\sin\varphi'_p} \tag{11}$$

where φ_{cs} is the critical state friction angle; φ_m is the mobilized friction angle; φ'_p is the peak dilation angle.

The adopted stress–dilatancy relationship serves as the link between shear hardening and volumetric hardening by relating the plastic shear strain increment to the plastic volumetric strain increment. In this formulation, its influence is mainly reflected in the evolution of radial effective stress and the corresponding mobilization of shaft resistance. The effect is expected to be limited during the initial elastic stage, more evident when shear and volumetric yielding develop simultaneously, and gradually reduced as the interface response approaches the critical state. Other stress–dilatancy relationships, such as Rowe-type or Bolton-type formulations, could also be introduced into the present framework if sufficient interface test data are available for calibration. The current form is adopted because it is consistent with the critical-state-based volumetric hardening mechanism and can be conveniently incorporated into the incremental double-hardening load-transfer model while preserving computational efficiency.

2.2.2. Flow Rules and Plastic Potential Functions

A non-associated flow rule is adopted for the plastic potential surface corresponding to the shear yield surface, and its plastic potential function g^s is defined as:

$$g^s = q - p'\frac{\sin\psi_m}{\frac{1}{\sqrt{3}}\sin\theta\sin\varphi' + \cos\theta} = 0 \tag{12}$$

An associated flow rule is adopted for the plastic potential surface corresponding to the volumetric yield surface, and its plastic potential function g^c is defined as:

$$g^c = q^2 - M^2 p'(p'_c - p') = 0 \tag{13}$$

2.2.3. Partitioning of Yield Surfaces and Loading Modes in the $p' - q$ Plane

The shear and volumetric yield surfaces of the proposed double-hardening constitutive model delineate the $p' - q$ stress plane into four distinct regions: I, II, III, IV. As illustrated in Figure 4, these regions represent the purely elastic zone, the independent volumetric yielding zone, the independent shear yielding zone, and the double yielding zone, where shear and volumetric yielding occur concurrently, respectively.

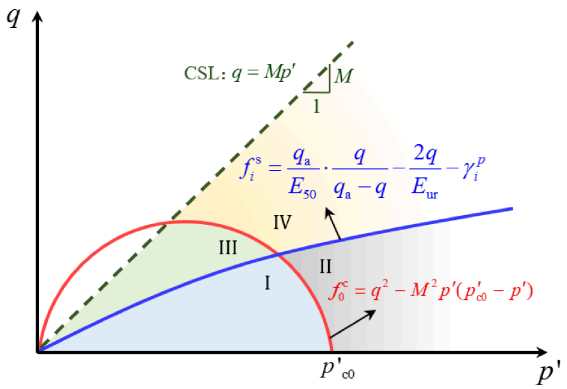


Figure 4. Schematic diagram of $p' - q$ plane division by shear and volumetric yield.

Figure 5 illustrates the loading modes and yield surface states within the $p' - q$ plane. As depicted in Figure 5a, when the stress point is situated within the shear yield surface, $f^s < 0$, the interface soil exhibits elastic behavior. Upon reaching the shear yield surface $f^s = 0$, sustained loading initiates further plastic deformation, leading to the outward expansion of the yield surface. In the case of neutral loading, the interface soil remains in a plastic state without accumulating additional plastic strain; conversely, unloading transitions the soil back into the elastic regime. The evolutionary characteristics of the volumetric yield surface under various loading modes, as shown in Figure 5b, follow analogous principles and are omitted here for brevity.

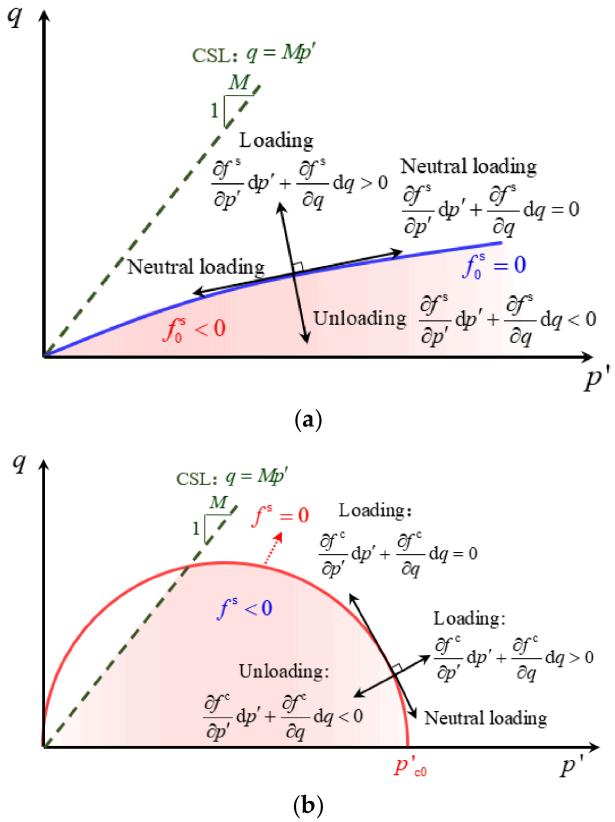


Figure 5. Schematic diagram of shear and volumetric yield surface loading modes and yield surface states: (**a**) Shear yield surface; (**b**) Volumetric yield surface.

Considering both the yield surface states and loading modes simultaneously, when the stress point is located inside both yield surfaces, the yield functions satisfy $f^s < 0$ and $f^c < 0$. Under this condition, the soil remains in the elastic state regardless of the loading

mode. When the stress point is located in region IV, where $f^{s} = 0$ and $f^{c} = 0$. If the loading increment is directed outward from both the shear and volumetric yield surfaces, the soil enters a plastic state characterized by the simultaneous expansion of both surfaces and the continuous accumulation of plastic strain. Conversely, if the loading direction is directed outward from the shear yield surface but inward (unloading) or tangentially (neutral loading) to the volumetric surface, only the shear yield surface expands, resulting in a state of purely shear yielding. Consequently, the mechanical behavior of the interface soil is jointly governed by the loading mode and the instantaneous state of the yield surfaces. The elastoplastic responses of the pile–soil interface under various loading scenarios are summarized in Table 1.

Table 1. Table of elastoplastic states of the contact interface under different yield surface states and loading modes.

Region	Yield Surface State	Loading Mode	Elastoplastic Behavior
I	$f^{s} < 0$ $f^{c} < 0$	Regardless of loading mode	Double elastic
II	$f^{s} < 0$ $f^{c} = 0$	$\frac{\partial f^{c}}{\partial p'}dp' + \frac{\partial f^{c}}{\partial q}dq < 0$ $\frac{\partial f^{c}}{\partial p'}dp' + \frac{\partial f^{c}}{\partial q}dq \geq 0$	Double elastic Volumetric yielding
III	$f^{s} = 0$ $f^{c} < 0$	$\frac{\partial f^{s}}{\partial p'}dp' + \frac{\partial f^{s}}{\partial q}dq < 0$ $\frac{\partial f^{s}}{\partial p'}dp' + \frac{\partial f^{s}}{\partial q}dq \geq 0$	Double elastic Shear yielding
IV	$f^{s} = 0$ $f^{c} = 0$	$\frac{\partial f^{s}}{\partial p'}dp' + \frac{\partial f^{s}}{\partial q}dq < 0$ $\frac{\partial f^{c}}{\partial p'}dp' + \frac{\partial f^{c}}{\partial q}dq < 0$ $\frac{\partial f^{s}}{\partial p'}dp' + \frac{\partial f^{s}}{\partial q}dq < 0$ $\frac{\partial f^{c}}{\partial p'}dp' + \frac{\partial f^{c}}{\partial q}dq \geq 0$ $\frac{\partial f^{s}}{\partial p'}dp' + \frac{\partial f^{s}}{\partial q}dq \geq 0$ $\frac{\partial f^{c}}{\partial p'}dp' + \frac{\partial f^{c}}{\partial q}dq < 0$ $\frac{\partial f^{s}}{\partial p'}dp' + \frac{\partial f^{s}}{\partial q}dq \geq 0$ $\frac{\partial f^{c}}{\partial p'}dp' + \frac{\partial f^{c}}{\partial q}dq \geq 0$	Double elastic Volumetric yielding Shear yielding Double yielding

2.3. Incremental Constitutive Formulation of the Pile–Soil Interface

2.3.1. Elastic Strain Increment

The elastoplastic deformation of the pile–soil interface comprises elastic and plastic components. Consequently, the total relative displacement increment at the interface can be partitioned into elastic and plastic strain increments, which are evaluated independently.

The elastic strain increment is calculated using Hooke's Law, which is expressed as:

$$\begin{bmatrix} d\varepsilon_{v}^{e} \\ d\gamma^{e} \end{bmatrix} = [D^{e}]_{2\times 2} \begin{bmatrix} dp' \\ dq \end{bmatrix} \tag{14}$$

where $[D]_{2\times 2}^{e}$ is expressed as:

$$[D^{e}]_{2\times 2} = \begin{bmatrix} \frac{3(1-2v)}{E} & 0 \\ 0 & \frac{2\sqrt{2}(1+v)}{3E} \end{bmatrix} \tag{15}$$

where μ is Poisson's ratio; E is the elastic modulus.

2.3.2. Plastic Strain Increment

When loading occurs within the double yielding region of the shear and volumetric yield surfaces (IV), the plastic strain increments of the soil are:

$$\mathrm{d}\gamma^{p} = \Lambda_1 \frac{\partial g^{\mathrm{s}}}{\partial q} + \Lambda_2 \frac{\partial g^{\mathrm{c}}}{\partial q} \tag{16}$$

$$\mathrm{d}\varepsilon_{\mathrm{v}}^{\mathrm{p}} = \Lambda_1 \frac{\partial g^{\mathrm{s}}}{\partial p'} + \Lambda_2 \frac{\partial g^{\mathrm{c}}}{\partial p'} \tag{17}$$

where Λ_1 and Λ_2 are the plastic multipliers.

According to the plastic consistency condition, by differentiating $f^{\mathrm{s}} = 0$ and $f^{\mathrm{c}} = 0$, combining Equations (5), (16), and (17), and expressing the result in matrix form:

$$\begin{bmatrix} a_{11} & a_{12} \\ a_{21} & a_{22} \end{bmatrix} \begin{bmatrix} \Lambda_1 \\ \Lambda_2 \end{bmatrix} = \begin{bmatrix} e_{11} & e_{12} \\ e_{21} & e_{22} \end{bmatrix} \begin{bmatrix} \mathrm{d}p' \\ \mathrm{d}q \end{bmatrix} \tag{18}$$

where:

$$a_{11} = -\frac{\partial f^{\mathrm{s}}}{\partial \gamma^{\mathrm{p}}} \frac{\partial g^{\mathrm{s}}}{\partial q} \tag{19}$$

$$a_{12} = -\frac{\partial f^{\mathrm{s}}}{\partial \gamma^{\mathrm{p}}} \frac{\partial g^{\mathrm{c}}}{\partial q} \tag{20}$$

$$a_{21} = -\frac{\partial f^{\mathrm{c}}}{\partial p'_{\mathrm{c}}} \frac{\partial g^{\mathrm{s}}}{\partial p'} \frac{(1+e_0)p'_{\mathrm{c}}}{\lambda - k} \tag{21}$$

$$a_{22} = -\frac{\partial f^{\mathrm{c}}}{\partial p'_{\mathrm{c}}} \frac{\partial g^{\mathrm{c}}}{\partial p'} \frac{(1+e_0)p'_{\mathrm{c}}}{\lambda - k} \tag{22}$$

$$e_{11} = \frac{\partial f^{\mathrm{s}}}{\partial p'} \tag{23}$$

$$e_{12} = \frac{\partial f^{\mathrm{s}}}{\partial q} \tag{24}$$

$$e_{21} = \frac{\partial f^{\mathrm{c}}}{\partial p'} \tag{25}$$

$$e_{22} = \frac{\partial f^{\mathrm{c}}}{\partial q} \tag{26}$$

Under the double yielding state presented in Table 1, Equation (18) is guaranteed to yield a unique solution for the plastic multipliers [39]. Therefore, the plastic volumetric strain increment $\mathrm{d}\varepsilon_{\mathrm{v}}^{\mathrm{p}}$ and the plastic shear strain increment $\mathrm{d}\gamma_{\mathrm{p}}$ of the soil are given as:

$$\begin{bmatrix} \mathrm{d}\varepsilon_{\mathrm{v}}^{\mathrm{p}} \\ \mathrm{d}\gamma^{\mathrm{p}} \end{bmatrix} = \begin{bmatrix} \frac{\partial g^{\mathrm{s}}}{\partial q} & \frac{\partial g^{\mathrm{c}}}{\partial q} \\ \frac{\partial g^{\mathrm{s}}}{\partial p'} & \frac{\partial g^{\mathrm{c}}}{\partial p'} \end{bmatrix} \begin{bmatrix} \Lambda_1 \\ \Lambda_2 \end{bmatrix} \tag{27}$$

By combining Equations (19) and (20), the relationship between the plastic strains, the mean stress p', and the deviatoric stress q is obtained as follows:

$$\begin{bmatrix} \mathrm{d}\varepsilon_{\mathrm{v}}^{\mathrm{p}} \\ \mathrm{d}\gamma^{\mathrm{p}} \end{bmatrix} = [D_4^{\mathrm{p}}]_{2\times 2} \begin{bmatrix} \mathrm{d}p' \\ \mathrm{d}q \end{bmatrix} \tag{28}$$

where:

$$[D_4^{\mathrm{p}}]_{2\times 2} = \begin{bmatrix} \frac{\partial g^{\mathrm{s}}}{\partial q} & \frac{\partial g^{\mathrm{c}}}{\partial q} \\ \frac{\partial g^{\mathrm{s}}}{\partial p'} & \frac{\partial g^{\mathrm{c}}}{\partial p'} \end{bmatrix} \begin{bmatrix} a_{11} & a_{12} \\ a_{21} & a_{22} \end{bmatrix}^{-1} \begin{bmatrix} e_{11} & e_{12} \\ e_{21} & e_{22} \end{bmatrix} \tag{29}$$

Similarly, the plastic strain increment $d\varepsilon_v^p$ and $d\gamma_p$ in region II is given as:

$$\begin{bmatrix} d\varepsilon_v^p \\ d\gamma^p \end{bmatrix} = [D_2^p]_{2\times 2} \begin{bmatrix} dp' \\ dq \end{bmatrix} \tag{30}$$

where:

$$[D_2^p]_{2\times 2} = \frac{1}{A_s} \begin{bmatrix} \frac{\partial f^s}{\partial p'} \frac{\partial g^s}{\partial p'} & \frac{\partial f^s}{\partial q} \frac{\partial g^s}{\partial p'} \\ \frac{\partial f^s}{\partial p'} \frac{\partial g^s}{\partial q} & \frac{\partial f^s}{\partial q} \frac{\partial g^s}{\partial q} \end{bmatrix} \tag{31}$$

where A_s is the shear hardening modulus, which is expressed as:

$$A_s = -\frac{\partial f^s}{\partial \gamma^p} \frac{\partial g^s}{\partial q} \tag{32}$$

Similarly, the plastic strain increment $d\varepsilon_v^p$ and $d\gamma_p$ in region III is given as:

$$\begin{bmatrix} d\varepsilon_v^p \\ d\gamma^p \end{bmatrix} = [D_3^p]_{2\times 2} \begin{bmatrix} dp' \\ dq \end{bmatrix} \tag{33}$$

where:

$$[D_3^p]_{2\times 2} = \frac{1}{A_c} \begin{bmatrix} \frac{\partial f^c}{\partial p'} \frac{\partial g^c}{\partial p'} & \frac{\partial f^c}{\partial q} \frac{\partial g^c}{\partial p'} \\ \frac{\partial f^c}{\partial p'} \frac{\partial g^c}{\partial q} & \frac{\partial f^c}{\partial q} \frac{\partial g^c}{\partial q} \end{bmatrix} \tag{34}$$

where A_c is the volumetric hardening modulus, which is expressed as:

$$A_c = -\frac{(1+e_0)p_c'}{\lambda - k} \frac{\partial f^c}{\partial p_c'} \frac{\partial g^c}{\partial p'} \tag{35}$$

2.3.3. Interface Constitutive Matrix

The total strain increment of the pile–soil interface soil is equal to the sum of the elastic strain increment and the plastic strain increment. By combining Equations (14), (21), (23), and (26), the total strain of the pile–soil interface is obtained as follows:

$$\begin{bmatrix} d\varepsilon_v^p \\ d\gamma^p \end{bmatrix} = [D^{ep}]_{2\times 2} \begin{bmatrix} dp' \\ dq \end{bmatrix} \tag{36}$$

where:

$$\left[D^{ep}\right]_{2\times 2} = [D^e] + \left[D_i^p\right] \tag{37}$$

2.4. Iterative Load-Transfer Algorithm for Axially Loaded Piles

2.4.1. Pile–Soil Interaction Mechanism

Under axial loading, the pile–soil interface undergoes plastic shear deformation once the shear stress mobilizes the shear strength of the soil. Moreover, the shear stress exerted on the surrounding soil mass diminishes as the radial distance from the pile axis increases. To rigorously characterize the deformation behavior and load-transfer mechanisms of the soil surrounding the pile, the soil is partitioned into two distinct domains: a shear deformation zone exhibiting elastoplastic behavior and an outer elastic zone where only linear elastic deformation prevails, as illustrated in Figure 6.

Under the applied axial load, soil particles within the shear deformation zone experience relative sliding and structural reconfiguration. These processes are frequently accompanied by complex mechanical phenomena, including compressive shear and plastic flow, which manifest as pronounced elastoplastic behavior. This localized soil region,

confined to a narrow annulus adjacent to the pile shaft, serves as the governing zone for the mobilization and evolution of shaft friction. In contrast, the elastic zone extends beyond the shear deformation boundary, where the induced shear strains are sufficiently small to be approximated as linear elastic deformation. Assuming that perfect bonding is maintained without relative interface slip within the bearing capacity range of the pile foundation [6], the total settlement of the vertically loaded pile, S_z, is expressed as:

$$S_z = S_{z,p} + S_{z,e} \tag{38}$$

where $S_{z,p}$ is the elastoplastic shear displacement of the soil in the shear deformation zone, which can be obtained through the double-hardening elastoplastic constitutive model; $S_{z,e}$ is the elastic shear displacement of the soil in the elastic zone.

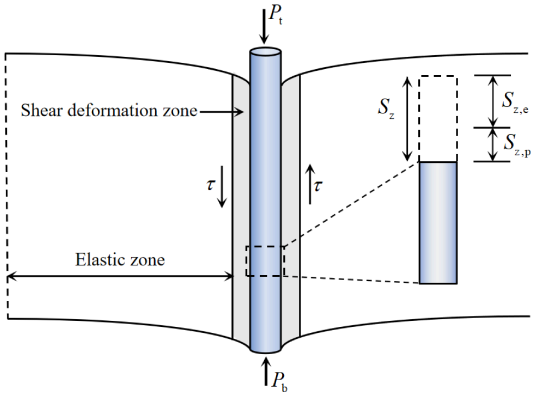


Figure 6. Schematic diagram of shear deformation in the soil surrounding the pile.

To simplify the calculations, the stress state of the soil surrounding the pile is idealized as follows: Since the stiffness of the pile is much greater than that of the surrounding soil, the lateral compression of the pile can be neglected, and the influence of σ'_θ is not considered. Given the axisymmetry of the load acting on the shear deformation zone, the tangential variations of $\tau_{r\theta}$ and $\tau_{\theta z}$ vanish. Therefore, the effects of $\tau_{r\theta}$ and $\tau_{\theta z}$ during the shearing process are ignored. Furthermore, by taking an extremely thin section of the soil surrounding the pile as the unit of analysis, the influence of the vertical effective stress σ'_z on the shearing process becomes negligible. Consequently, the stress state in the shear deformation zone can be simplified to a two-dimensional problem. Thus, only the effects of the radial effective stress σ'_r and the shear stress τ_{rz} are considered, as illustrated in Figure 7 [2,6].

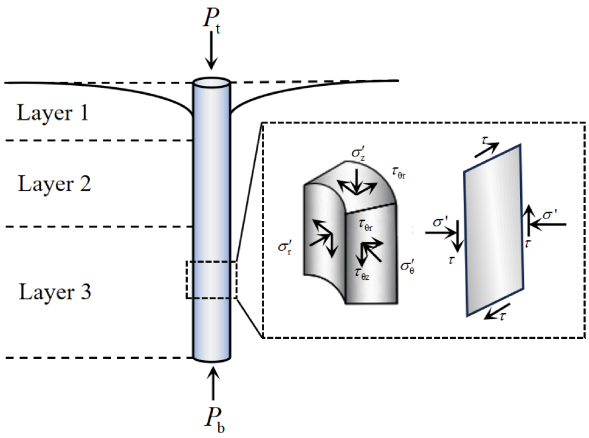


Figure 7. Schematic of the stress state of a soil element at the pile-soil interface.

2.4.2. Soil Displacement in the Elastic Zone

The load-transfer method is conceptualized by discretizing the pile into a series of discrete elastic elements, each interfaced with the surrounding soil through nonlinear spring analogies. These springs are employed to characterize the constitutive relationship between the shaft resistance τ and the shear displacement S_b, as well as the interaction between the tip resistance σ_b and the corresponding tip displacement S_b. The discrete representation of the pile foundation and the associated free-body diagram for a representative elastic element are illustrated in Figure 8.

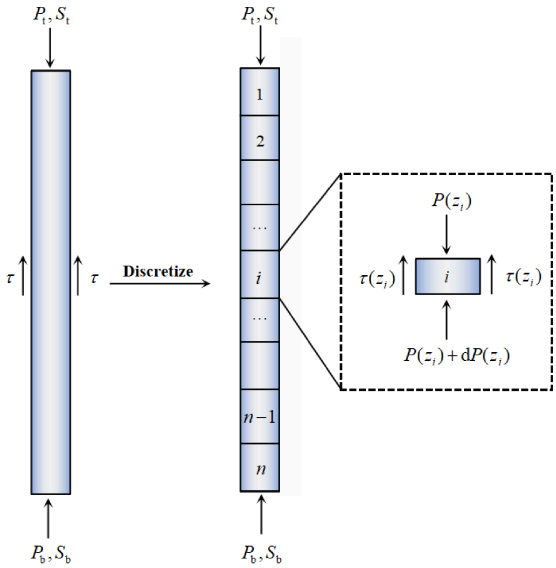


Figure 8. Schematic diagram of load-transfer method.

To rigorously characterize the stress-dependency of the elastic shear modulus at the pile–soil interface, a stress-level-dependent formulation [40] is adopted. This approach effectively captures the evolution of the interface's elastic shear stiffness with respect to the instantaneous stress state, with the governing expression defined as:

$$G = \left[1 - m_g \left(\frac{\tau_{rz}}{\tau_{rz,max}}\right)^{n_g}\right] G_0 \tag{39}$$

where τ_{rz} denotes the shear stress of the soil at a distance from the pile center; G_0 is the maximum shear modulus of the soil; $\tau_{rz,max}$ is the maximum shear stress of the soil, which can be calculated using an elastoplastic constitutive model; m_g and n_g are experimental fitting parameters.

The shear strain of the soil at an arbitrary point in the elastic zone surrounding the pile element can be expressed as:

$$\gamma_{rz} = \frac{r_0 \tau_{rz,0}}{Gr} \tag{40}$$

where G is the elastic shear modulus of the soil; r_0 is the radius of the pile; $\tau_{rz,0}$ is the shear stress at the pile–soil interface.

By integrating Equation (33) within the elastic zone, the shear deformation of the soil under shear stress can be obtained:

$$S_{z,e} = r_0 \tau_{rz,0} \int_{r0}^{r_m} \frac{1}{Gr} dr \tag{41}$$

where r_m is the influence radius of the elastic zone of the soil around the pile. It is assumed that the shear stress at this distance from the pile center is approximately zero:

$$r_m = 2.5L\rho(1-\mu) \tag{42}$$

where L is the pile length; ρ is the non-homogeneity factor; μ is the Poisson's ratio of the soil.

Substituting the modified elastic shear modulus expression Equation (32) into Equation (34), the shear deformation of the soil in the elastic zone is obtained as:

$$S_{z,e} = \frac{r_0\tau_{rz,0}}{G_0 n_g}\ln\left[\frac{\left(\frac{r_m}{r_0}\right)^{n_g} - m_g\left(\frac{\tau_{rz,0}}{\tau_{max}}\right)^{n_g}}{1 - m_g\left(\frac{\tau_{rz,0}}{\tau_{max}}\right)^{n_g}}\right] \tag{43}$$

2.4.3. Pile Toe Load–Displacement Relationship

The overall bearing capacity of the pile is significantly governed by the base resistance, which demonstrates a pronounced nonlinear correlation with the soil deformation at the pile tip. Utilizing the hyperbolic model [41], the relationship for the pile base resistance is formulated as follows:

$$\sigma_b = \frac{S_b}{m_b + n_b S_b} \tag{44}$$

where σ_b is the pile base resistance; S_b is the compression displacement at the pile tip; m_b is the reciprocal of the initial compression modulus of the soil at the pile tip; n_b is the reciprocal of the ultimate capacity of the soil at the pile tip. The expressions for m_b and n_b are:

$$m_b = \frac{1}{k_b} = \frac{\pi r_0(1-\mu)}{4G_b} \tag{45}$$

$$n_b = \frac{1}{q_{bf}} = \frac{R_{bf}}{q_{bu}} \tag{46}$$

where $1/k_b$ is the initial compression modulus of the soil at the pile tip, which can be estimated using the shear modulus G_b; q_{bf} is the ultimate resistance of the soil at the pile tip; q_{bu} is the ultimate bearing capacity of the soil at the pile tip; R_{bf} is the failure ratio, where:

$$q_{bu} = N_q\sigma'_z \tag{47}$$

where N_q is the bearing capacity factor, taken as 9.7; σ'_z is the vertical effective stress of the soil at the pile tip.

In this model, a small incremental settlement is prescribed for the i-th pile segment. The displacement component of this segment is determined according to the pile base load–settlement relationship. Subsequently, the proposed double-hardening constitutive model is implemented to evaluate the shaft displacement of the i-th segment, thereby yielding the corresponding skin friction and local load-transfer response. By enforcing static equilibrium conditions, the axial force and displacement at the upper boundary of the i-th segment are derived. These results are then propagated through each pile element by ensuring deformation compatibility. Ultimately, the comprehensive load–settlement curve for the pile head is generated. The detailed computational procedure is illustrated in the algorithmic flowchart in Figure 9.

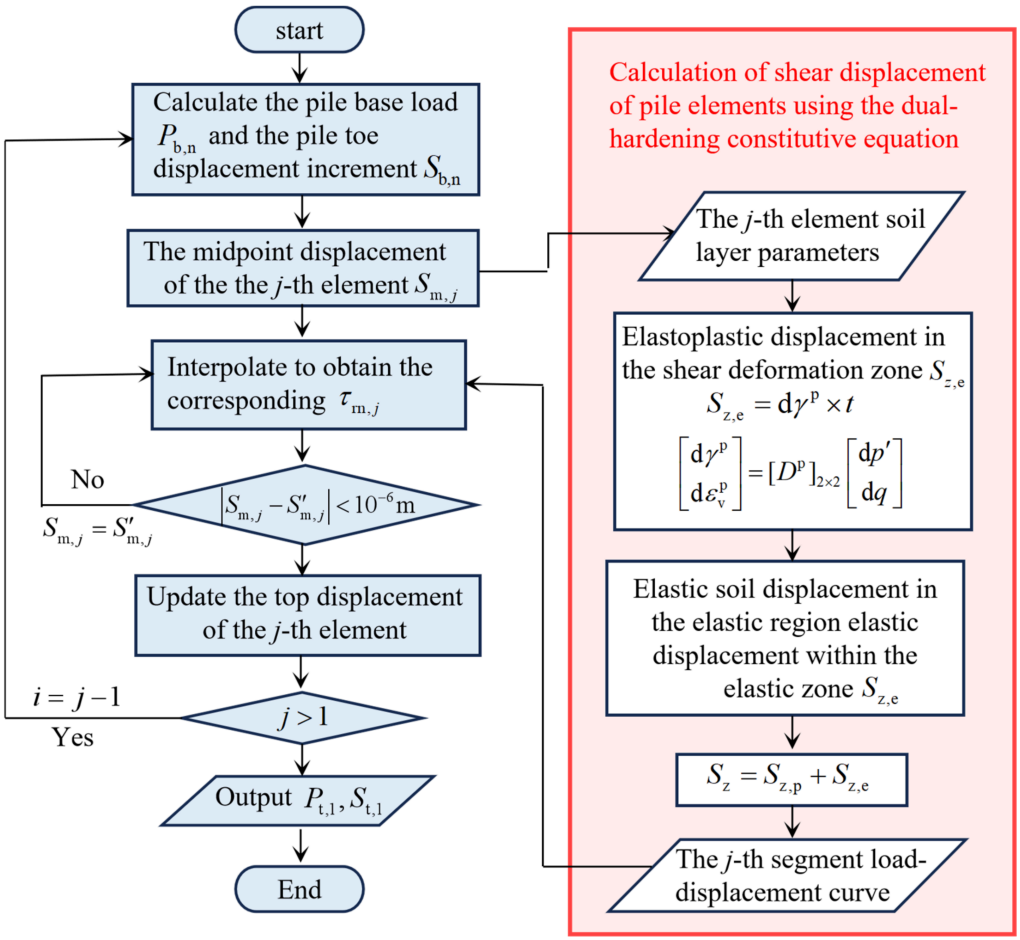


Figure 9. The calculation flowchart of pile load-settlement curve based on the load-transfer method.

3. Results

3.1. Validation Against Interface Direct Shear Tests

To validate the applicability and predictive fidelity of the proposed double-hardening elastoplastic constitutive model, the numerical results were benchmarked against experimental data from direct shear tests [42]. During the loading sequence, a monotonic increase in the shear stress τ_{vh} on the shear plane is assumed. The kinematic relationship between the incremental shear displacement dz and the resulting shear strain increment $d\gamma_{vh}$ is defined as follows:

$$dz = d\gamma_{vh} \times t \tag{48}$$

where t denotes the thickness of the shear deformation zone, a characteristic parameter intrinsically linked to the soil particle size. This thickness typically ranges from 3 mm to 30 mm. Specifically, the shear zone thickness in Norwegian clay is approximately 3–5 mm; in contrast, for sandy soils, it corresponds to roughly 10–15 times the mean grain size [43].

The simulation results for the direct shear tests, utilizing the proposed double-hardening elastoplastic model, were derived through Equations (29) and (41) in accordance with the computational procedure outlined in Figure 9. A comparative analysis between the current model predictions and the experimental results reported by Mortara et al. (2007) [44] and Benz (2007) [45] is presented in Figures 10 and 11. Furthermore, the geotechnical parameters employed for this validation process are tabulated in Table 2.

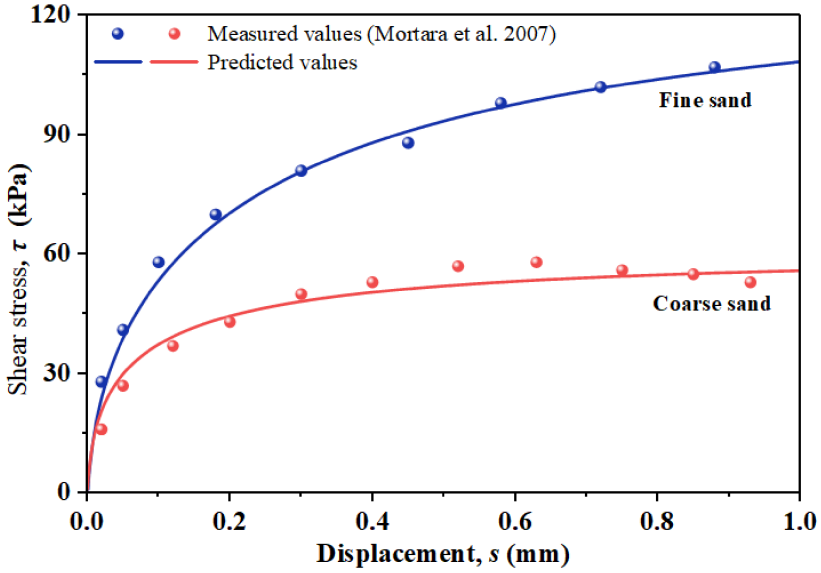


Figure 10. Comparison of model predictions with direct shear tests on sand–steel interfaces [44].

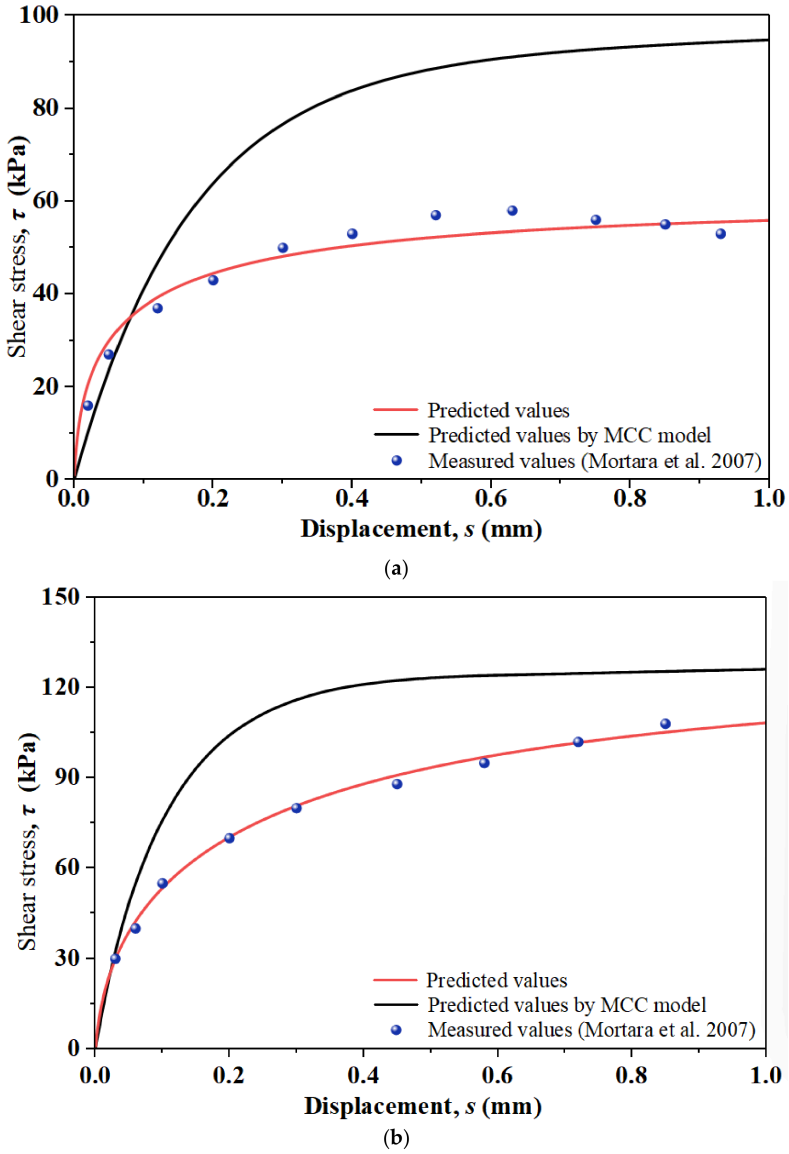


Figure 11. Comparison between model predictions and direct shear tests on sand–steel interfaces: (**a**) Coarse sand; (**b**) Fine sand [44].

Table 2. Soil parameters in direct shear tests of sand–steel interfaces.

Soil Parameters	Coarse Sand: GT10	Fine Sand: GT40
E_{50}^{ref}(kPa)	30,000	20,000
$E_{\mathrm{ur}}^{\mathrm{ref}}$(kPa)	80,000	60,000
p^{ref}(kPa)	100	100
μ	0.25	0.25
m	0.65	0.65
R_{f}	0.9	0.9
c'(kPa)	0	0
$\varphi'(^\circ)$	20	34
$\varphi'_{\mathrm{p}}(^\circ)$	0	0
e_0	0.65	0.74
λ	0.02	0.03
κ	0.01	0.005
t (mm)	20	20

As illustrated in Figure 10, both coarse and fine sands exhibit prominent shear hardening characteristics at the sand–steel interface under an initial normal stress of 150 kPa, with the shear stress monotonically increasing alongside displacement. At a displacement of 1.0 mm, the shear stress for fine sand reaches approximately 130 kPa, significantly exceeding the 68 kPa observed for coarse sand; this discrepancy is primarily attributable to the superior interlocking and frictional mechanisms inherent in fine sand particles. For the coarse sand–steel interface, the model predictions demonstrate high fidelity with the experimental data, accurately capturing the evolutionary trend of the interface's shear deformation. Although the model slightly underestimates the shear stress of fine sand during the incipient shearing stage, it successfully characterizes the more pronounced yet gradual shear deformation behavior of the fine sand interface. Overall, the proposed double-hardening model effectively captures the elastoplastic features of the pile–soil interface, yielding robust trend predictions with high numerical accuracy.

As illustrated in Figure 11, under a normal stress of 150 kPa, the Modified Cam-clay (MCC) model yields a reasonably accurate approximation of the initial shear stiffness; however, it significantly diverges from the experimental observations during the subsequent evolutionary phase. This discrepancy is primarily attributable to the fact that the MCC model exclusively accounts for volumetric hardening while disregarding the influence of shear hardening on the soil's mechanical response. Consequently, it is incapable of adequately capturing the shear hardening effect induced by particle interlocking in sand, leading to an overestimation of the interface stiffness and strength. Conversely, the proposed model rigorously characterizes the stress–strain behavior of the interface by integrating dual hardening mechanisms. For coarse sand, the model faithfully represents the shear hardening behavior by employing an appropriate non-associated flow rule. This approach effectively depicts the progression of shear stress with increasing shear strain, resulting in a developmental trend that shows high fidelity to the experimental data. For fine sand, the predicted curves also exhibit strong correlation with the experimental results, demonstrating that the proposed model is highly robust in characterizing the shear deformation behavior of sand–structure interfaces.

3.2. Case Study Validation: Large-Diameter Bored Pile in Bangkok Soft Clay

To evaluate the validity of the proposed model, Pile T1 from the field study by Brenner et al. (1981) [46] on the bearing characteristics of large-diameter bored piles in soft Bangkok clay was selected for validation. Pile T1 has a length of 25.8 m and a diameter of 1.0 m, with a pile elastic modulus E_{50} of 45 GPa. As illustrated in Figure 12, the pile penetrates a

soft clay stratum approximately 15 m thick and is seated in the underlying stiff clay layer, with the pile toe situated within the latter. The geotechnical parameters for the respective soil layers are tabulated in Table 3. The bearing capacity of this pile is predominantly governed by shaft resistance, whereas the contribution of base resistance remains relatively minor, exemplifying a typical friction pile. Figure 12 compares the measured pile-head settlements with the predicted load–displacement curves under various loading scenarios following installation.

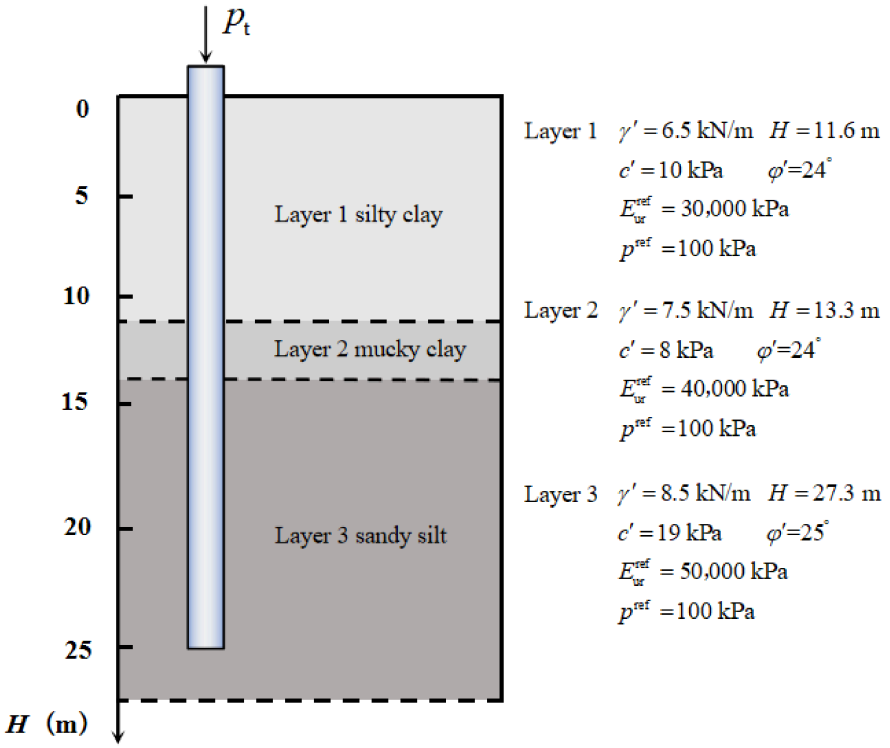


Figure 12. Schematic diagram of soil strata for bored cast-in-place piles in Bangkok soft soils.

Table 3. Geotechnical parameter of layer t1 for pile foundations in Bangkok soft marine clays.

Layer	1	2	3
h (mm)	0–11.6	11.6–13.3	13.3–27.3
γ' (N/m)	6.5	7.5	8.5
E_{50}^{ref}(kPa)	6000	80,000	10,000
E_{ur}^{ref}(kPa)	30,000	40,000	50,000
p^{ref}(kPa)	100	100	100
μ	0.3	0.3	0.3
m	0.7	0.7	0.7
R_f	0.9	0.9	0.9
c'(kPa)	10	8	19
φ'(°)	24	24	25
φ'_p(°)	0	0	0
e_0	1.6	1.3	0.9
λ	0.22	0.1	0.045
κ	0.056	0.017	0.009
OCR	1	1	1
G_0(kPa)	38,400	40,000	45,000
n_g	0.5	0.35	0.25
m_g	0.95	0.95	0.99
t (mm)	3	3	3

As illustrated in Figure 13, by integrating the proposed double-hardening interface constitutive model into the load-transfer method, the mechanical behavior of the pile–soil interface is accurately characterized across various shear deformation stages. This results in a high degree of concordance between the predicted and measured load–settlement characteristics throughout the loading process. At low load levels ($P_t < 3$MN), the load–settlement relationship displays quasi-linear behavior, as the majority of the pile–soil interface remains in the elastic regime, with only a limited zone near the ground surface entering a plastic state. As the load reaches intermediate levels (3MN $\leq P_t \leq$ 4MN), the intensified load-transfer causes the interface along the upper and middle sections to transition into the elastoplastic stage; concurrently, the tip resistance begins to be mobilized to share the load despite the lower shaft remaining elastic. Finally, at high load levels ($P_t >$ 4MN), the yielding of the lower interface and the full mobilization of the tip bearing capacity result in a sharp increase in pile-head settlement, manifested as a pronounced steepening of the curve.

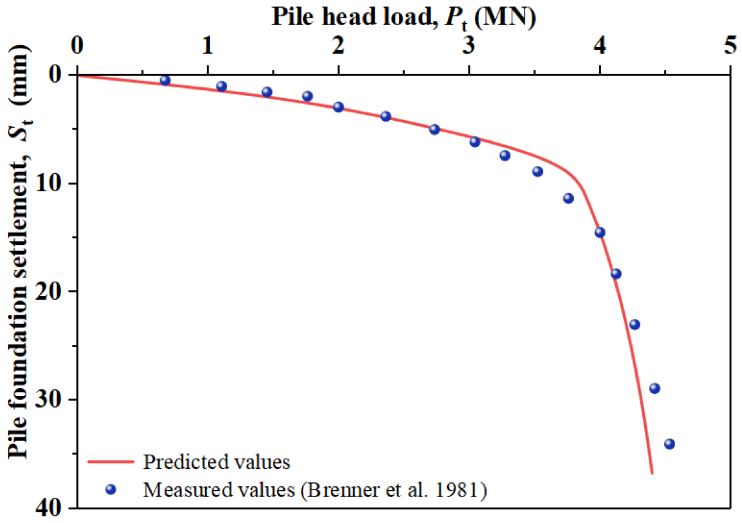


Figure 13. Comparison of load-settlement curves for bored cast-in-place piles in Bangkok soft marine clays [46].

3.3. Case Study Validation: Pile Foundation in Shanghai Zhoupu Soft Clay

Static load test results for a pile foundation in soft clay in the Zhoupu area of Shanghai, as reported by Li et al. (2017) [47], were utilized for model validation. The experimental program featured pre-stressed concrete (PSC) piles with a diameter of 0.35 m, an embedment length of 30 m, and an elastic modulus of 40 GPa. Although the original study monitored three piles at intervals of 7, 25, and 60 days post-installation, the data from the 60-day test were selected for this validation to ensure that the surrounding soil had reached a sufficient degree of consolidation and stabilized mechanical properties. As illustrated in the stratigraphic profile in Figure 14, the site is predominantly composed of saturated soft clay, silty clay, and mucky clay. Based on Li et al. (2017) [47] and associated research on the geomechanically properties of Shanghai soil strata [48], the geotechnical parameters for the test site are tabulated in Table 4.

As illustrated in Figure 15, the model provides an accurate prediction of the load-settlement curve throughout the entire loading process. The predicted values show good agreement with the experimental data, further demonstrating the capability of the proposed model to reasonably characterize the load-settlement behavior of pile foundations. At the low-load stage, the model accounts for the variation of the elastic shear modulus of the surrounding soil in relation to the shear stress level, enabling a more precise prediction of the interface deformation during the initial elastic phase. At high-load levels, the

double-hardening constitutive model effectively incorporates both the shear hardening and volumetric hardening of the pile–soil interface, accurately describing its shear deformation behavior. By integrating these features with the load-transfer method, the model reasonably predicts the load-transfer mechanism of the pile shaft. Consequently, it can accurately capture the non-linear load-settlement characteristics and the phenomenon of abrupt settlement (plunging behavior) occurring at high levels.

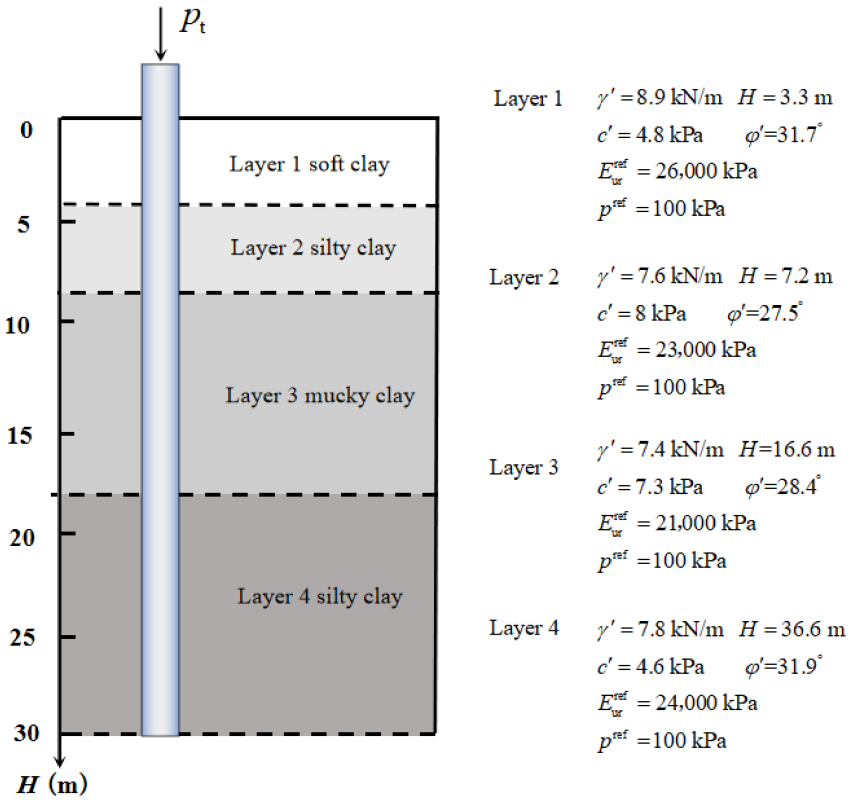


Figure 14. Stratigraphic map of clay soil layers for pile foundation in the Shanghai area.

Table 4. Soil layer parameters for pile foundation in soft clay, Zhoupu area, Shanghai.

Layer	1	2	3	4
h (mm)	0–3.3	3.3–7.2	7.2–16.6	16.6–36.6
γ' (N/m)	8.9	7.6	7.4	7.8
E_{50}^{ref}(kPa)	4500	3700	3500	4200
E_{ur}^{ref}(kPa)	26,000	23,000	21,000	24,000
p^{ref}(kPa)	100	100	100	100
μ	0.3	0.3	0.3	0.3
m	0.65	0.65	0.65	0.65
R_f	0.9	0.9	0.9	0.9
c'(kPa)	4.8	8.0	7.3	4.6
$\varphi'(^\circ)$	31.7	27.5	28.4	31.9
$\varphi'_p(^\circ)$	0	0	0	0
e_0	1.1	1.2	1.2	1.1
λ	0.09	0.22	0.21	0.14
κ	0.02	0.05	0.04	0.03
OCR	1.1	1.1	1.1	1.1
G_0(kPa)	29,500	32,200	25,800	27,800
n_g	0.1	0.1	0.1	0.1
m_g	0.99	0.99	0.99	0.99
t (mm)	3	3	3	3

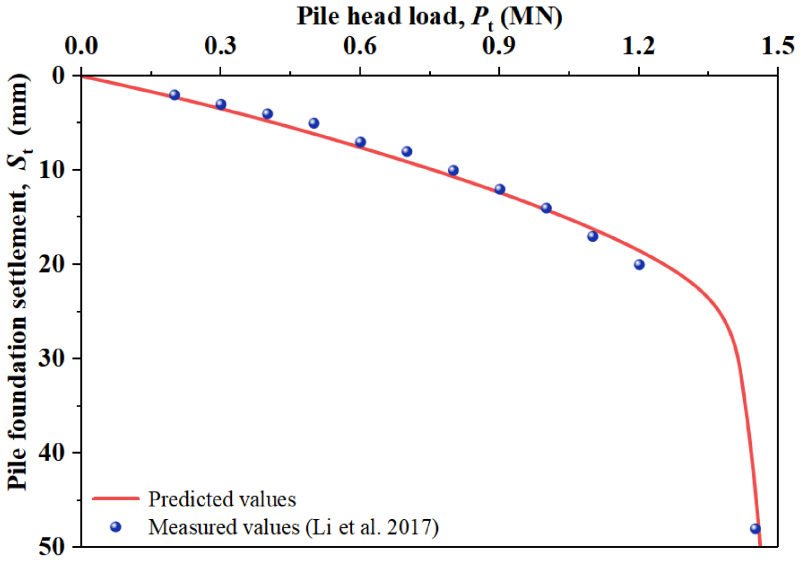


Figure 15. Comparison of load-settlement curves for pile foundations in Shanghai clay [47].

3.4. Quantitative Evaluation of Prediction Accuracy

To further evaluate the predictive accuracy of the proposed model, a quantitative comparison was conducted between the calculated results and the measured data from the interface direct shear tests and field-scale static pile load tests. Three statistical indicators were adopted: the mean absolute percentage error (MAPE), the maximum relative error, and the coefficient of determination (R^2). The MAPE evaluates the average relative prediction error, and R^2 indicates the overall agreement between the predicted and experimental responses.

The quantitative results are summarized in Table 5. For the interface direct shear tests, the proposed model reproduces the nonlinear shear stress–displacement response of both coarse and fine sand–steel interfaces with low prediction errors. For the field-scale pile load tests, the calculated pile-head load–settlement curves also show good agreement with the measured results, indicating that the model can reliably capture the progressive mobilization of shaft resistance and the nonlinear settlement response under increasing axial load. Overall, the quantitative indicators confirm that the proposed double-hardening elastoplastic load-transfer model provides stable and accurate predictions across both interface-scale and field-scale validation cases.

Table 5. Quantitative evaluation of prediction accuracy for different validation cases.

Case	MAPE (%)	Maximum Relative Error (%)	R^2
Direct shear test: coarse sand	3.2	5.8	0.985
Direct shear test: fine sand	2.9	5.2	0.988
Bangkok bored pile	4.8	7.6	0.962
Shanghai Zhoupu pile	4.3	7.1	0.971

4. Discussion

4.1. Model Performance Under Different Validation Cases

The primary feature of the proposed model is its ability to smoothly and rigorously capture progressive yielding and multi-stage load-transfer. By integrating the Hardening Soil (HS) shear-hardening mechanism and the Modified Cam-clay (MCC) volumetric-hardening mechanism through a stress–dilatancy relationship, the model distinguishes the transitions among elastic response, independent shear hardening, independent volumetric hardening, and coupled double-yielding states.

In the interface direct shear tests, the model accurately reproduced the nonlinear shear stress–displacement response of sand–steel interfaces. In the field-scale pile load tests, the model also captured the progressive mobilization of shaft resistance and the nonlinear pile-head load–settlement behavior under increasing axial load. These results indicate that the proposed formulation can consistently describe both local pile–soil interface behavior and global pile foundation response.

4.2. Comparison with Conventional Load-Transfer Models

Compared with conventional empirical or hyperbolic load-transfer models, the proposed model provides a more physically interpretable prediction framework because the load-transfer response is governed by the coupled evolution of shear hardening, volumetric hardening, and radial effective stress at the pile–soil interface, rather than by purely curve-fitting parameters. Conventional models can reproduce the general shape of load–settlement curves after calibration, but their parameters usually have limited physical meaning and are difficult to transfer across different soil conditions. In contrast, the proposed double-hardening elastoplastic model explicitly describes the progressive transition from elastic response to independent hardening and coupled double-yielding states, thereby providing a clearer mechanical explanation for stiffness degradation and nonlinear settlement development. Compared with more detailed three-dimensional elastoplastic finite element approaches, the proposed model does not aim to reproduce the full stress and deformation fields around the pile. Instead, it provides a simplified one-dimensional framework that captures the key interface hardening mechanisms governing the pile-head load–settlement response. Therefore, the proposed method offers a balance between the empirical simplicity of conventional load-transfer curves and the mechanical rigor of advanced numerical models.

The quantitative results in Table 5 further support the effectiveness of the proposed model. For the interface direct shear tests, the MAPE values are 3.2% and 2.9% for coarse sand and fine sand, respectively, and the corresponding R^2 values reach 0.985 and 0.988. For the field-scale pile load tests, the MAPE values are 4.8% for the Bangkok bored pile and 4.3% for the Shanghai Zhoupu pile, with R^2 values of 0.962 and 0.971, respectively. In all validation cases, the maximum relative error remains below 7.6%. These results indicate that the proposed model maintains stable prediction accuracy across both interface-scale and field-scale problems.

Therefore, although conventional load-transfer models may provide acceptable curve fitting for specific cases, the proposed model is more effective in terms of both mechanical interpretability and predictive stability. It not only reproduces the measured nonlinear response with low prediction errors but also explains the underlying elastoplastic load–transfer mechanism through the coupled shear-hardening and volumetric-hardening formulation. This advantage is particularly important for predicting pile behavior in complex soil profiles, where the progressive mobilization of shaft resistance and the degradation of interface stiffness cannot be adequately represented by simple empirical transfer functions.

4.3. Applicability and Limitations of the Proposed Model

The major advantage of the proposed model lies in its ability to link local pile–soil interface behavior with the global load–settlement response of axially loaded piles. By incorporating coupled shear hardening, volumetric hardening, and radial effective stress evolution into the load-transfer framework, the model can reproduce the shear hardening behavior observed in interface tests and the progressive mobilization of shaft resistance in layered soil profiles, such as those observed in the Bangkok and Shanghai field cases.

The proposed model also has practical computational advantages. Since the pile is discretized only along the depth direction, the computational scale is mainly controlled by the number of pile elements. Compared with three-dimensional elastoplastic finite element analysis, which requires spatial discretization of the pile, surrounding soil, and interface, the proposed one-dimensional framework provides a more efficient alternative for routine prediction of pile-head load–settlement response, although it is not intended to replace detailed three-dimensional analysis when full stress and deformation fields are required.

From an engineering perspective, the proposed method can be used for interpreting static pile load tests, calibrating load-transfer parameters, and evaluating the bearing performance of axially loaded piles in soft or layered soil deposits. This is relevant to pile-supported structures such as high-rise buildings, long-span bridges, port structures, and transportation infrastructure, where accurate prediction of pile settlement is important for deformation control and serviceability assessment.

However, several limitations should be acknowledged. First, the model parameters require calibration from laboratory tests, field load tests, or reliable geotechnical data, and uncertainties in stiffness, strength, dilatancy, and volumetric hardening parameters may affect the predicted load–settlement response. Second, the current formulation mainly focuses on monotonic axial loading of single piles and does not explicitly consider cyclic degradation, pile–group interaction, or time-dependent consolidation effects. Third, although soil layering can be considered by assigning different parameters to different layers, highly heterogeneous, anisotropic, or structure-dependent soils and installation-induced disturbance may require additional site-specific calibration or coupling with more advanced constitutive descriptions. These issues should be further investigated in future studies through parameter sensitivity analysis, uncertainty evaluation, cyclic loading extensions, and improved modelling of complex ground and installation effects.

5. Conclusions

This study developed a double-hardening elastoplastic load-transfer model for predicting the load–settlement response of axially loaded piles. The proposed model provides a physically interpretable framework for describing the coupled shear and volumetric deformation mechanisms of the pile–soil interface and for linking local interface behavior with the global response of pile foundations.

From the theoretical perspective, a double-hardening elastoplastic constitutive model was established for the pile–soil interface. The Hardening Soil (HS) model was adopted to describe shear hardening, while the Modified Cam-clay (MCC) model was introduced to characterize volumetric hardening. These two hardening mechanisms were coupled through the stress–dilatancy relationship, allowing the model to represent the interaction between shear deformation, volumetric plastic strain, and radial effective stress evolution at the pile–soil interface.

The proposed formulation divides the stress plane into elastic, shear-hardening, volumetric-hardening, and coupled double-hardening regions according to the yield surface state and loading direction. Based on the plastic consistency condition and corresponding flow rules, the incremental constitutive equations for different regions were derived. This enables the progressive transition from elastic response to independent hardening and coupled double-yielding states to be described within a unified elastoplastic framework.

From the methodological perspective, the interface constitutive model was embedded into a conventional one-dimensional load-transfer framework. The elastoplastic shear displacement in the shear deformation zone adjacent to the pile and the elastic displacement of the surrounding soil were combined through deformation compatibility. Therefore,

the proposed method retains a clear elastoplastic mechanical basis while maintaining computational efficiency for pile load–settlement analysis.

The proposed model was validated using pile–soil interface direct shear tests and field-scale static pile load tests. For the direct shear tests, the predicted shear stress–displacement curves agreed well with the measured nonlinear responses of the sand–steel interfaces. For the field pile load tests, the calculated pile-head load–settlement curves captured the nonlinear settlement development and rapid stiffness degradation under increasing axial load. The quantitative evaluation further showed that the MAPE values were lower than 5%, the maximum relative errors were below 7.6%, and the R^2 values ranged from 0.962 to 0.988.

From the engineering application perspective, the proposed model can be used as a theoretical and practical tool for interpreting static pile load tests, calibrating load-transfer parameters, evaluating bearing performance, and predicting settlement development of axially loaded piles in soft or layered soil deposits. It is particularly relevant to pile-supported structures such as high-rise buildings, long-span bridges, port structures, and transportation infrastructure, where accurate prediction of pile load–settlement behavior is important for deformation control and serviceability assessment.

Nevertheless, several limitations should be acknowledged. The present model is mainly formulated for monotonic axial loading of single piles, and its predictive performance depends on the calibration quality of interface and soil parameters. For cyclic loading, pile groups, highly heterogeneous or anisotropic soils, and cases with significant installation-induced disturbance or residual stresses, additional mechanisms such as cyclic degradation, pile–pile interaction, anisotropic or structure-dependent constitutive descriptions, and post-installation stress correction may be required. Future work may further incorporate parameter sensitivity and uncertainty analyses, extend the formulation to cyclic and group-pile conditions, and couple the proposed load-transfer framework with more detailed descriptions of installation effects and complex ground conditions.

Author Contributions: Conceptualization, Y.L.; Software, Y.L., X.W. and S.Q.; Validation, H.L. and X.W.; Investigation, Y.L., X.W. and S.Q.; Resources, Y.L., X.W., J.Y. and L.L.; Data curation, Y.Z., H.L., X.W. and L.L.; Writing—original draft, Y.L.; Writing—review and editing, Y.Z., H.L., S.Q. and J.Y.; Visualization, Y.Z., H.L., S.Q. and J.Y.; Supervision, Y.Z. and J.Y. All authors have read and agreed to the published version of the manuscript.

Funding: This research received no external funding.

Data Availability Statement: The original contributions presented in this study are included in the article. Further inquiries can be directed to the corresponding author.

Conflicts of Interest: Authors Yexun Li, Xian Wang, Song Qiu, were employed by the company Third Harbour Engineering Corporation Ltd. The remaining authors declare that the research was conducted in the absence of any commercial or financial relationships that could be construed as a potential conflict of interest.

Nomenclature

p'	Mean effective stress
q	Deviatoric stress
E_{50}	Reference values of loading modulus
E_{ur}	Unloading-reloading modulus
p^{ref}	Confining pressure
c'	Effective cohesion of the soil
φ'	Effective angle of internal friction
m	Exponent parameter fitted from triaxial test results

q_a	Allowable deviatoric stress
q_f	Ultimate deviatoric stress
R_f	Failure ratio
θ	Lode angle of stress
γ^p	Plastic shear strains
f_0^s	Initial shear yield surface of the soil
p'_c	Yield stress
M	Critical state stress ratio
e_0	Initial void ratio
λ	Compression index
k	Swelling index
$d\gamma^p$	Plastic shear strain increment
$d\varepsilon_v^p$	plastic volumetric strain increment
φ_{cs}	Critical state friction angle
φ_m	Mobilized friction angle
φ'_p	Peak dilation angle
Λ_1, Λ_2	Plastic multipliers
$S_{z,p}$	Elastoplastic shear displacement
$S_{z,e}$	Elastic shear displacement
σ'_z	Vertical effective stress
σ'_r	Radial effective stress
τ_{rz}	Shear stress of the soil at a distance from the pile center
G_0	Maximum shear modulus of the soil
$\tau_{rz,max}$	Maximum shear stress of the soil
m_g, n_g	Experimental fitting parameters
ρ	Non-homogeneity factor
μ	Poisson's ratio of the soil
N_q	Bearing capacity factor
E_{50}^{ref}	Reference secant loading modulus
E_{ur}^{ref}	Reference unloading–reloading modulus

References

1. Wang, M.S.; Zhou, X.Y.; Hu, Y.X. Studies on Contact Model of Soil–Pile Dynamic Interaction. *Chin. J. Geotech. Eng.* **2005**, *27*, 616–620.
2. Abou-Samra, G.; Silvestri, V.; Desjardins, S.L.; Labben, R. Drained–Undrained Shaft Resistance of Piles in Soft Clays. *Int. J. Civ. Eng.* **2021**, *19*, 115–125.
3. Gylland, A.; Jostad, H.; Nordal, S. Experimental Study of Strain Localization in Sensitive Clays. *Acta Geotech.* **2014**, *9*, 221–240.
4. Jiang, M.J.; Wang, F.Z.; Zhu, H.H. Shear Band Formation in Ideal Dense Sand in Direct Shear Test by Discrete Element Analysis. *Rock Soil Mech.* **2010**, *31*, 253–257+298.
5. Poulos, H.G.; Davis, E.H. The Settlement Behaviour of Single Axially Loaded Incompressible Piles and Piers. *Géotechnique* **1968**, *18*, 351–371. [CrossRef]
6. Randolph, M.F.; Wroth, C.P. Analysis of Deformation of Vertically Loaded Piles. *J. Geotech. Eng. Div.* **1978**, *104*, 1465–1488. [CrossRef]
7. He, S.M. Modified Layer-Summation Based on Elastoplastic Theory. *Rock Soil Mech.* **2003**, *24*, 88–92. [CrossRef] [PubMed]
8. Liang, F.Y.; Jia, Y.J.; Ding, Y.J.; Huang, M.S. Experimental Study on Parameters of HSS Model for Soft Soils in Shanghai. *Chin. J. Geotech. Eng.* **2017**, *39*, 269–278.
9. Wang, X.J. A Load-Transfer Method for Analyzing Side-Grouting Uplift Piles Based on Pile Tests. *Rock Soil Mech.* **2015**, *36*, 321–326.
10. Lin, P.; Li, S.C.; Zhang, Q.Q.; Li, L.P.; Zhang, Q.; Xu, Z.; Sun, C. Development of Software for Nonlinear Analysis of Single Pile Response Based on Load-Transfer Method and Its Application. *Rock Soil Mech.* **2013**, *34*, 375–382.
11. Li, Z.Q. Some Problems on Load-Transfer and Bearing Capacity of Friction Piles. *Rock Soil Mech.* **1990**, *4*, 1–12.
12. Peng, F.L.; Lei, L.; Bai, X.Y. Double Hardening Characteristics of Sand and Its Elastoplastic Constitutive Model. *Chin. J. Rock Mech. Eng.* **2011**, *30*, 373–381.

13. Chen, R.P.; Zhou, W.H.; Cao, W.P.; Chen, Y. Improved Hyperbolic Model of Load-Transfer for Pile–Soil Interface and Its Application in Study of Negative Friction of Single Piles Considering Time Effect. *Chin. J. Geotech. Eng.* **2007**, *6*, 824–830.
14. Kraft, L.M.; Ray, R.P.; Kagawa, T. Theoretical t–z Curves. *J. Geotech. Eng. Div.* **1981**, *107*, 1543–1561. [CrossRef]
15. Zhu, H.; Chang, M.F. Load-Transfer Curves along Bored Piles Considering Modulus Degradation. *J. Geotech. Geoenviron. Eng.* **2002**, *128*, 764–774. [CrossRef]
16. Roscoe, K.H.; Burland, J.B. On the Generalized Stress–Strain Behavior of "Wet" Clay. In *Engineering Plasticity*; Cambridge University Press: Cambridge, UK, 1968; pp. 535–560.
17. Roscoe, K.H.; Thurairajah, A.; Schofield, A.N. Yielding of Clays in States Wetter than Critical. *Géotechnique* **1963**, *13*, 211–240. [CrossRef]
18. Xu, M.; Song, E.X. A Strain Hardening Model for Rockfills. *Rock Soil Mech.* **2010**, *31*, 2967–2972+2986.
19. Schanz, T.; Vermeer, P.A.; Bonnier, P.G. The Hardening Soil Model: Formulation and Verification. In *Beyond 2000 in Computational Geotechnics*; Routledge: Abingdon, UK, 1999; pp. 281–296.
20. Shen, Z.J. Double Hardening Model for Clay. *Rock Soil Mech.* **1995**, *16*, 1–8.
21. Yu, J.L.; Sun, X.; Yu, Y.Z. Applicability of Modified Double Hardening Model to Structured Soil. *J. Guangxi Univ. Nat. Sci. Ed.* **2009**, *34*, 289–292.
22. Bateman, A.H.; Crispin, J.J.; Vardanega, P.J.; Mylonakis, G.E. Theoretical t–z Curves for Axially Loaded Piles. *J. Geotech. Geoenviron. Eng.* **2022**, *148*, 04022052. [CrossRef]
23. Sharo, A.; Al-Shorman, B.; Bani Baker, M.; Nusier, O.; Alawneh, A. New Approach for Predicting the Load–Displacement Curve of Axially Loaded Piles in Sand. *Case Stud. Constr. Mater.* **2022**, *17*, e01674. [CrossRef]
24. Li, L.; Lai, N.; Zhao, X.; Zhu, T.; Su, Z. A Generalized Elastoplastic Load-Transfer Model for Axially Loaded Piles in Clay: Incorporation of Modulus Degradation and Skin Friction Softening. *Comput. Geotech.* **2023**, *161*, 105594. [CrossRef]
25. Pham, T.A.; Nadimi, S.; Sutman, M. Softening-Based Interface Model and Nonlinear Load–Settlement Response Analysis of Piles in Saturated and Unsaturated Multi-Layered Soils. *Comput. Geotech.* **2024**, *171*, 106331. [CrossRef]
26. Mao, S.; Zheng, C.; Zhang, Z.; Wang, G.; Chen, J. Analytical Solution for Axially Loaded Floating Pipe Piles in Homogeneous Elastic Soil Layer. *Ocean Eng.* **2024**, *309*, 118509. [CrossRef]
27. Zhou, H.; Li, Y.; Sheil, B. Load-transfer Model for Vertically Loaded Non-Circular Piles. *Comput. Geotech.* **2025**, *177*, 106843. [CrossRef]
28. Cesaro, R.; Di Laora, R.; Mandolini, A. Shaft Resistance of Bored Piles in Sand. *Acta Geotech.* **2025**. [CrossRef]
29. Nguyen, T.; Ly, D.-K.; Shiau, J.; Nguyen-Dinh, P. Optimizing Load–Displacement Prediction for Bored Piles with the 3mSOS Algorithm and Neural Networks. *Ocean Eng.* **2024**, *304*, 117758. [CrossRef]
30. Wang, T.; Fan, H.; Wang, K.R.; Zhou, G.; Wang, L. A Unified Constitutive Model for Dual-Yield Surface for Warm Frozen Soil and Its Verification. *Chin. J. Geotech. Eng.* **2025**, *47*, 135–143.
31. Li, B.; Zhang, Y.; Liu, H.; Wang, Z.; Zhao, H. Determination of Stiffness and Strength Parameters for the Hardening Soil Model Based on the Simplicial Homology Global Optimization and Triaxial Compressive Test. *Sci. Rep.* **2025**, *15*, 10413. [CrossRef] [PubMed]
32. Lashkari, A. Elastoplastic Constitutive Modelling of Soil–Structure Interfaces under Monotonic and Cyclic Loading. *Int. J. Numer. Anal. Methods Geomech.* **2012**, *36*, 1397–1427.
33. Zhang, B.; Wang, J. Macroscopic Behaviour and Mesoscopic Mechanism of Shear Strength Characteristics of Pile–Soil Interface under Cyclic Loading. *Constr. Build. Mater.* **2021**, *272*, 121954.
34. Lim, J.K.; Kim, H.W. Investigation of the Load–Settlement Response of Piles in Sand Using an Interface Constitutive Model. *Comput. Geotech.* **2022**, *142*, 104562.
35. Cui, C.; Meng, K.; Xu, C.; Wang, B.; Xin, Y. Vertical Vibration of a Floating Pile Considering the Incomplete Bonding Effect of the Pile–Soil Interface. *Comput. Geotech.* **2022**, *150*, 104894. [CrossRef]
36. Sun, Z.C.; Chu, J.; Xiao, Y. Formulation and Implementation of an Elastoplastic Constitutive Model for Sand–Fines Mixtures. *Int. J. Numer. Anal. Methods Geomech.* **2021**, *45*, 2682–2708. [CrossRef]
37. Yang, C.-J.; Cai, Z.-Y.; Zhu, X.; Fan, K.-F.; Li, G.; Liu, C.-Y. Implementation and Application of a State-Dependent Sand Model in Finite Element Analysis. *Geotech. Geol. Eng.* **2025**, *43*, 426. [CrossRef]
38. Rowe, P.W. The Stress–Dilatancy Relation for Static Equilibrium of an Assembly of Particles in Contact. *Proc. R. Soc. Lond. Ser. A. Math. Phys. Sci.* **1962**, *269*, 500–527. [CrossRef]
39. Yin, Y.Q. Stress Space and Strain Space Formulation of the Elasto-Plastic Constitutive Relations for Singular Yield Surface. *Acta Mech. Sin.* **1986**, *2*, 169–177. [CrossRef]
40. Fahey, M.; Carter, J.P. A Finite Element Study of the Pressuremeter Test in Sand Using a Nonlinear Elastic Plastic Model. *Can. Geotech. J.* **1993**, *30*, 348–362. [CrossRef]
41. Tang, X.S.; Li, D.Q.; Zhou, C.B.; Phoon, K.K. Probabilistic Analysis of Load–Displacement Hyperbolic Curves of Single Pile Using Copula. *Rock Soil Mech.* **2012**, *33*, 171–178.

42. Hashemi, A.; Sutman, M.; Abuel-Naga, H. Thermomechanical Response of Kaolin Clay–Concrete Interface in the Context of Energy Geostructures. *Can. Geotech. J.* **2023**, *60*, 380–396. [CrossRef]
43. Chakraborty, T.; Salgado, R.; Basu, P.; Prezzi, M. Shaft Resistance of Drilled Shafts in Clay. *J. Geotech. Geoenviron. Eng.* **2013**, *139*, 548–563. [CrossRef]
44. Mortara, G.; Mangiola, A.; Ghionna, V.N. Cyclic Shear Stress Degradation and Post-Cyclic Behaviour from Sand–Steel Interface Direct Shear Tests. *Can. Geotech. J.* **2007**, *44*, 739–752. [CrossRef]
45. Benz, T. *Small-Strain Stiffness of Soils and Its Numerical Consequences*; Institut für Geotechnik, Universität Stuttgart: Stuttgart, Germany, 2007.
46. Brenner, R.P.; Promboon, S. Large-Diameter Bored Piles in Bangkok Clay. In *Proceedings of the International Conference on Soil Mechanics and Foundation Engineering*; International Society for Soil Mechanics and Geotechnical Engineering (ISSMGE): Londin, UK, 1981; Volume 2, pp. 815–818.
47. Li, L.; Li, J.; Sun, D.; Gong, W. Semi-Analytical Approach for Time-Dependent Load–Settlement Response of a Jacked Pile in Clay Strata. *Can. Geotech. J.* **2017**, *54*, 1682–1692. [CrossRef]
48. He, P.; Wang, W.D.; Xu, Z.H. Empirical Correlations of Compression Index and Swelling Index for Shanghai Clay. *Rock Soil Mech.* **2018**, *39*, 3773–3782.

Disclaimer/Publisher's Note: The statements, opinions and data contained in all publications are solely those of the individual author(s) and contributor(s) and not of MDPI and/or the editor(s). MDPI and/or the editor(s) disclaim responsibility for any injury to people or property resulting from any ideas, methods, instructions or products referred to in the content.